J. Fluid Mech. (2000), *vol.* 425, *pp.* 1–29. Printed in the United Kingdom

An experimental investigation of the vertical temperature structure of homogeneous stratified shear turbulence

By KURT H. KELLER AND CHARLES W. VAN ATTA†

Department of Mechanical and Aerospace Engineering, University of California, San Diego, La Jolla, CA 92093, USA

(Received 7 September 1999 and in revised form 21 April 2000)

The vertical temperature structure of homogeneous stratified shear turbulence is investigated using new rapid vertical temperature measurements in a thermally stratified wind tunnel. Six cases of gradient Richardson number, $Ri_g = N^2/(\mathrm{d}\bar{U}/\mathrm{d}z)^2$, where N is the Brunt–Väisälä frequency ($N^2 = (g/\bar{T})\mathrm{d}\bar{T}/\mathrm{d}z$), are studied, spanning a range $0.015 \leqslant Ri_g \leqslant 0.5$. Three- to five-hundred high-resolution temperature profiles are made for several streamwise stations for each case of Ri_g. These measurements are supplemented with standard fixed-point, Eulerian measurements of streamwise and vertical velocity fluctuations and temperature fluctuations and with an eight-point vertical rake of temperature probes using standard hot-wire and cold-wire techniques. Vertical profiles uniquely enable the computation of available potential energy (APE), Thorpe scales (L_{Th}), and the diapycnal flux (ϕ_d), as well as one-dimensional vertical wavenumber temperature spectra. These quantities are compared with Eulerian measurements of turbulent kinetic energy (KE), potential energy (PE), and buoyancy flux. It is found that the one-dimensional vertical wavenumber temperature spectrum contains more energy at smaller scales compared to the horizontal spectrum, owing in part to shear distortion, which leads to larger mean square vertical gradients of fluctuating temperature as compared to mean square horizontal gradients. The combination of shear and stratification, especially for cases where the turbulence decays with evolution, accelerates the evolution toward small-scale anisotropy compared to just shear or just stratification. It is found that in highly stratified cases, the diapycnal flux can persist after buoyancy flux has collapsed to negligible values, indicating enhanced heat transfer without turbulent mixing. For low Ri_g, large-scale vertical advection creates both high local temperature gradients and regions of static instability. Associated with the regions of instability is APE, which grows relative to KE for the least stratified cases. For high Ri_g, the turbulence evolves to a wavelike state, containing some counter gradient fluxes and unstable patches. This wavelike state has higher heat flux efficiency than the more turbulent states owing to the low dissipation but relatively high diapycnal flux.

1. Introduction

1.1. *Motivation*

The vertical structure of stratified turbulent flows has been investigated for many years in the ocean by temperature profiles and microstructure studies. Similar studies

† Also Scripps Institution of Oceanography, La Jolla, CA 92093, USA.

have been made in atmospheric flows. The vertical structure reveals the overall anisotropic properties of the geophysical turbulence and emphasizes the development of high-gradient regions and unstable regions.

Although *in situ* investigations of geophysical turbulence are required to have any measurement of the mixing in the ocean or atmosphere, the utility of these measurements is still not perfectly understood. This has led to the development of new theoretical frameworks, such as background potential energy (Winters *et al.* 1995) or isopycnal coordinate systems (Gregg 1987), to better understand the information contained in microstructure measurements. Recent numerical investigations have tried to use some of these ideas to better understand the energetics associated with a potential energy field (Winters & D'Asaro 1994; Staquet 2000), but a significant gap still exists in the understanding of how to use these measurements to determine the required quantities. An example of this difficulty is the reliance on the Osborn–Cox model (Osborn & Cox 1972) which uses dissipation measurements to measure the buoyancy flux indirectly. This model uses the assumption that the turbulence is in a steady state. However, without knowledge of the age of the turbulence (time since the initial overturn) or in cases where significant velocity shear exists, the steady-state assumption is inherently invalid.

Other more fundamental difficulties derive from the notion of a background density profile, as compared to a mean density profile. Winters *et al.* (1995) argue that the background density profile, the density profile obtained by adiabatic reordering of a density field to its minimum potential energy state, is changed, not by buoyancy fluxes, which are reversible, but by irreversible diapycnal fluxes. Therefore, a direct measure of the changes in large water masses is best measured directly through diapycnal fluxes. Given this argument, we might question the utility of measuring the buoyancy flux, an indirect measure of the actual irreversible mixing, versus the diapycnal flux, for the purpose of measuring diffusivities. Some indications of the problems in the calculating of diffusivities using the Osborn–Cox model are discussed by Davis (1994) who notes that the diffusivities predicted by large-scale measurements are 10 times greater than the measured diffusivities using the Osborn–Cox model and microstructure measurements.

The lack of significant experimental and numerical investigations directly into the vertical structure, especially in homogeneous turbulence, is a primary motivation for this study. Fundamentally, we would like to compare the information contained in the vertical measurements to the standard fixed-point measurements usually used in laboratory studies. Quantities such as vertical mean square gradients, vertical one-dimensional spectra, and vertical integral scales are all fundamental to a thorough understanding of these anisotropic flows. Additionally, new information can be obtained about the properties of microstructure measurements by evaulating the techniques used for microstructure measurements in a laboratory environment.

1.2. *Previous investigations*

The use of vertical measurements in experimental studies extends back many years in inhomogeneous flows, and has elucidated the tendency for generating high vertical density gradients and the final collapse of the turbulence into narrow mixed layers. Vertical density measurements have been extensively used for studying stratified mixing layers (Thorpe 1973). More recently, Taylor (1992) investigated breaking events in an internal wave field using vertical sampling. Using particle image velocimetry, Chomaz, Bonneton & Hopfinger (1993) studied the breakdown into different layers of a coherent sphere wake in a stratified fluid.

The collapse of three-dimensional homogeneous turbulence has been studied for specific cases in which the forcing is predominately aligned in the horizontal. Fincham, Maxworthy & Spedding (1996) investigated the long-time evolution of quasi-two-dimensional turbulence generated by vertically aligned bars passed through a stratified fluid. Park, Whitehead & Gnanadaskian (1994) similarly used a vertical rod to stir a stratified fluid for studying the evolution toward a layered density structure. Numerical investigations of unsheared homogeneous stratified turbulence have attempted to quantify the evolution toward a layered structure by using a Craya–Herring decomposition in which vortical modes and wave modes can be explicitly separated. Métais & Herring (1989), and later Staquet & Godeferd (1998) have shown that the vortical modes tend to dominate the flow energetically for long evolution. The interaction of these vortical modes at different heights is envisaged as a source of large vertical gradients of both velocity and density (Fincham *et al.* 1996). Godeferd & Cambon (1994) show that triadic interaction with vortical modes results in an irreversible anisotropy.

Experimental investigations which study the evolution from fully three-dimensional turbulence to the layered structure have not yet been carried out, owing to the difficulty of the experiment. However, Thoroddsen (1991) found, for evolution times $Nt/2\pi \approx 1$, significant anisotropy in small-scale structures (N is the Brunt–Väisälä frequency, and t is time). Itsweire (1984) successfully measured vertical profiles of density in a salt-stratified water tunnel, but only used these measurements to compare the Thorpe scales to other scales of the turbulence.

Investigations into the vertical structure of sheared, stratified turbulence are even less numerous. For shear flows, it is expected that the small scales of the velocity field will be isotropic for large enough Reynolds numbers, and that the large scales might be distorted by the mean shear (Tavoularis & Corrsin 1981*a*). However, some surprising phenomena have been found at small scales, even for high Reynolds numbers, such as counter gradient fluxes, where small buoyant parcels of fluid return to their neutral positions. This effect is thought to be especially important for large Prandtl or Schmidt numbers, in which diffusion of density is relatively slow compared to viscous diffusion. Gerz, Howell & Mahrt (1994) and Gerz & Schumann (1996) have investigated the mechanism for density microfronts, in which local regions of high-density gradients exist, postulating that horseshoe-vortex pairs are responsible for these structures. They theorize that two oppositely oriented horseshoe vortices advect fluid through their own legs, creating high gradients where the advected fluid meets.

Some indications are that for truly homogeneous turbulence, the details are not important for parameterizing the mixing by the turbulence at low enough Ri_g. Holt, Koseff & Ferziger (1992), Jacobitz, Sarkar & Van Atta (1997) and others have found a kind of self-similar evolution characterized by exponential energy evolution and constant mixing efficiencies. For flows in which homogeneity is not certain or when the ambient conditions are not known, as is the case in ocean microstructure studies (Dillon 1982; Gregg 1987), a self-similar framework is not necessarily helpful. Instead, one must obtain detailed measurements of the events which make up mixing in stratified flows in controlled laboratory environments to better understand the ocean processes. This type of investigation is comparable to investigations of coherent structures in jets and mixing layers where coherent structures control the dominant mixing events.

The plan of this paper is as follows. The experimental set-up is described in § 2. The results are presented in § 3. The results are discussed and some conclusions are explained in § 4. General conclusions are presented in § 5.

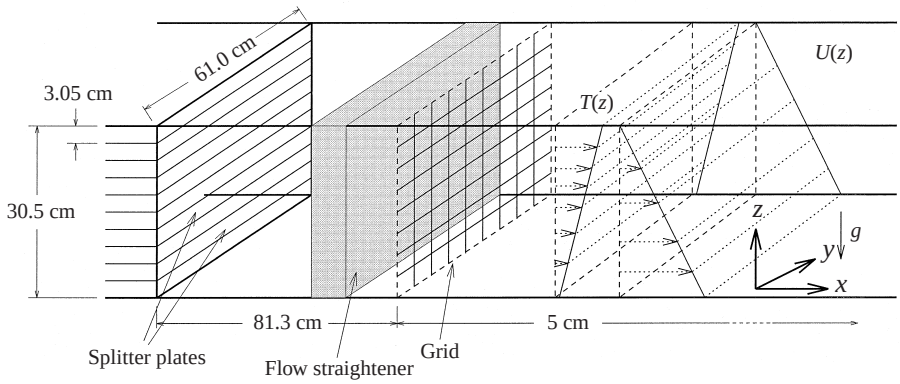

FIGURE 1. Schematic of the stratified shear wind tunnel. Mean velocity shear is negative, so high speeds are on the bottom. The flow straightener ensures that the flow passing through the 2.54 cm mesh grid is devoid of large scales originating at the splitter plates.

2. Experimental set-up

2.1. *Tunnel*

A 10-layer thermally stratified wind tunnel generates the mean flow used in this investigation. This tunnel was initially used by Piccirillo & Van Atta (1997) and is described in detail in Piccirillo & Van Atta (1996). The mean flow is generated in each layer independently, by controlling individual blowers and heaters in each layer. The flow within the different layers merges together about 80 cm upstream of the test section. A diagram of the tunnel is shown in figure 1. The tunnel test section dimensions are 5 m long by 60 cm wide by 30 cm high.

Some modifications of the tunnel have been carried out to improve its controllability, homogeneity, and the range of mean flows that can be generated. The improvements include a new inlet design which takes flow from each blower into individual layers. The new inlet minimizes drag and helps controllability. With the new inlets, a new large blower has been installed to power the lowest layer. This new blower has enabled mean shear rates of as high as 9.5 s^{-1}, which is about twice as large as the shear rates used in Piccirillo & Van Atta (1997). Also, having higher flow rates on the lowest layer enables better homogeneity by minimizing boundary-layer effects. An aluminium honeycomb flow straightener has also been added, placed about 10 cm upstream from the test section, to eliminate the coherent structures which develop at the shear layers where pairs of layers merge. Though the honeycomb greatly improved the homogeneity of the flow, it also generally lowered the microscale Reynolds number.

2.2. *Mean flow properties*

Six cases of gradient Richardson number, $Ri_g = 0.015$, 0.055, 0.095, 0.135, 0.25, 0.5, were studied. For each case, a 2.54 cm biplanar grid initiated the turbulence at the beginning of the test section. The initial microscale Reynolds number, $Re_\lambda = q\lambda/\nu$, where q is the total r.m.s turbulent velocity, λ is the Taylor microscale, $\lambda = (\overline{u^2}/\overline{(\partial u/\partial x)^2})^{1/2}$, and ν is the kinematic viscosity, was about 30 for each case. Depending on the flow conditions, Re_λ might grow or decay from that value. For $Ri_g = 0.015$, $Re_\lambda \approx 90$ by the end of the evolution. In contrast, for $Ri_g = 0.5$, $Re_\lambda \approx 20$ by the end of the evolution.

The mean profiles of velocity and temperature were measured at 7 streamwise stations for every case using a Pitot tube and slow response platinum resistance

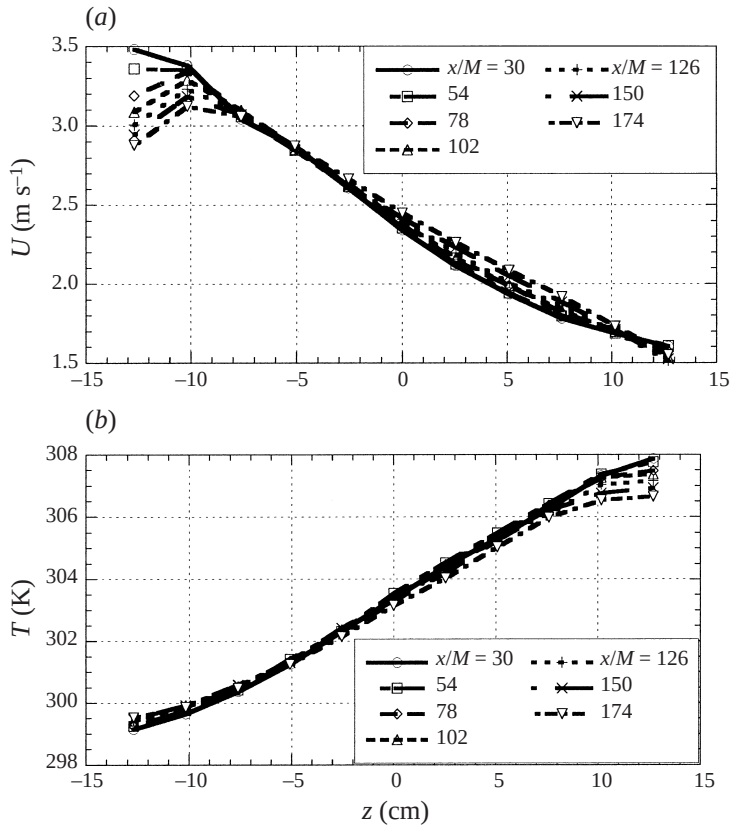

FIGURE 2. Mean profile evolution of velocity and temperature for $Ri_g = 0.015$. Mixing both straightens the profiles and flattens the gradients. Some boundary effects are evident, but the central 15 cm is unaffected.

probe. The evolution of these profiles is shown for one case in figure 2. The tunnel floor and roof were set to expand slightly to account for boundary-layer growth. However, the mixing of momentum and heat by the turbulence produces a slow evolution of the mean gradient of velocity and temperature. As a result, Ri_g evolves, since it depends inversely on the square of the velocity gradient, but linearly on the temperature gradient. Local values of velocity gradient and temperature gradient were used for every measurement station. These values were found by fitting a low-order polynomial curve to the measured mean gradients at the seven stations and then calculating local values using the fitted curve. Note that the different cases will be referred to by their initial values of Ri_g, thereby indicating the relative stability of the flow, but local values Ri_g are used for all computations.

2.3. *Vertical measurements*

The vertical measurements of temperature comprise the core measurement used in this study. Much of the experimental detail can be found in Keller & Van Atta (2000), in which the vertical traverse is explained and many other details are provided. Here, we will focus on the most relevant details only.

The vertical measurements are made with a resolution of about 0.085 mm over the span of the tunnel, from bottom to top. The measurements are made at equally spaced

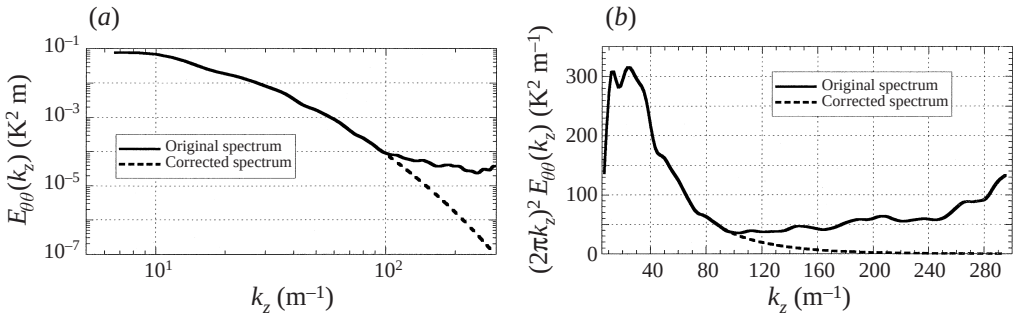

FIGURE 3. Examples of spectral correction for the noise tail exist in some measurements. The choice of the correction is not critical, since only 10% of the contribution is in this tail region. (*a*) Original and corrected power spectrum; (*b*) original and corrected dissipation spectrum.

intervals using an encoder to trigger measurements. This spatial resolution is much finer than actually needed, and therefore the measurements are subsequently digitally filtered to more appropriate resolutions. The probe is accelerated from rest to about 13 m s^{-1} and then back to rest within the confines of the tunnel, about 36 cm. Only vertical measurements in the central 15 cm of the tunnel, where the probe velocity is never less than 12 m s^{-1}, are used for calculations. The total time of measurement for each vertical sample is about 0.01 s, which gives effectively instantaneous profiles. For all but one case, 500 profiles were taken at each station (for $Ri_g = 0.25$, only 300 profiles were measured). The voltages were digitized with 16-bit precision, which is judged to be a minimum for this type of measurement.

The temperature measurements are made using standard cold-wire methods, as described by Haugdahl & Lienhard (1988). The response of the cold-wire bridge is estimated to be about 30 kHz, well above the thermal response of the cold wire itself. The cold-wire probe is a modified Dantec 55P1 single-wire probe, where a platinum wire is soldered to the prongs. For most measurements, the platinum wire was 0.625 μm diameter, with a length of 0.7 mm. The response of this size wire is estimated to be about 6.5 kHz (LaRue, Deaton & Gibson 1975) at 10 m s^{-1}, which corresponds to a spatial resolution of about 1.5 mm. Kolmogorov scales are estimated to be no less than 0.5 mm, for these flows, so 1.5 mm resolution should be sufficient. To test this issue, measurements were also made with 0.4 mm long, 0.25 μm diameter wires for $Ri_g = 0.25, 0.135, 0.5$. No significant differences were found in measured quantities, such as mean square gradients.

Some noise was evident at the very smallest scales in the highest stratification case ($Ri_g = 0.5$). This noise, which resembled intermittent spikes, was probably due to the electromagnetic noise emitted from the servo motor which powered the traverse. A comparison of vertical profiles from thick and thin wires showed that the spikes were made negligible by using the thinner wires, probably because the signal-to-noise ratio of the thinner wires is greater than that of the thicker wires. The thin wires did have some other high-frequency noise due to wire vibration which contributed additional noise. However, in all cases, the noise corrupted signals at scales much smaller than the peak of the dissipation spectrum. As a result of the noise problems, measurement for $Ri_g = 0.5$ were made using the thick wire (0.625 μm) for $x/M = 30, 54, 78$ and using the thin wire 0.25 μm for $x/M = 102, 126, 150, 174$. For all other measurements, the 0.625 μm wires were used.

In order to compute estimates of the mean square vertical temperature gradients

from vertical wavenumber spectra in which the dissipation spectrum was corrupted by some noise, the noise in the spectrum was removed by fitting a curve with the form $\exp(-k_z^2)$ to the smooth portion of the curve, and extended to small scales. This correction, illustrated in figure 3, was only used for the measurement of mean square gradients for $Ri_g = 0.5$ and the thin wire ($x/M = 102, 126, 150, 174$). The shape of the correction curve compared favourably with the shape of spectra where no noise was evident. In practice, owing to the low energy in this portion of the spectrum, the shape of the correction is not critical, and any errors are probably smaller than other experimental errors.

For the calculation of other quantities, such as Thorpe scales or APE, directly from the vertical profiles, the profiles are smoothed first using a low-pass filter with a cutoff which matches the point at which the spectrum falls off significantly.

2.4. *Standard measurements*

Standard X-wire and cold-wire measurements are made at several streamwise stations (with spacing of 15–30 cm). The X-wire and cold wire are placed close together, with cold wire aligned vertically. The X-wire, aligned for measurement of streamwise and vertical velocity, is a Dantec 55P11 probe, with wire length 1.25 mm. The cold wire is 0.625 μm diameter of length 0.7 mm, as described above. The X-wires are powered by an AN2000 anemometer by AAlabs. At each streamwise station, 1 024 000 simultaneous measurements at 5 kHz are made of the three voltages, which are subsequently converted to two velocities and one temperature via calibration laws. The calibration laws used to calculate velocity are derived by Lienhard (1988), with some modifications as detailed in Keller (1999). The cold wire has a linear calibration law. Calibration constants for each run are obtained using an external calibration jet in which the velocities and temperatures are varied to span the necessary range. Typical error in the calibration law is about 0.1%, based on the calibration measurements. Additional errors can be expected in the turbulence measurements owing to such complications as mean velocity gradient and limited spatial resolution relative to the small scales of the turbulence.

2.5. *Rake measurements*

The cold-wire rake consists of a vertical array of 8 cold-wire probes separated by 6.35 mm. 1 024 000 simultaneous measurements at 5 kHz are taken at 15 streamwise stations. The rake measurements will primarily be used for visualization purposes, but such measurements can also be used for direct calculation of two-dimensional autocorrelations and two-dimensional power spectra. The rake measurements are converted into temperature isocontour plots using *Tecplot*.

3. Results

3.1. *Turbulence characteristics*

Some turbulence characteristics of the flows are presented here, as they represent the types of flow to be studied with vertical profiles.

The velocities are decomposed into a mean $\bar{U}$, and fluctuating part, (u, v, w), with mean velocity gradient, $S = \mathrm{d}\bar{U}/\mathrm{d}z$, where the overbar indicates a mean quantity. Similarly, the temperature is decomposed into a mean $\bar{T}$ and fluctuation θ, with mean temperature gradient, $S_T = \mathrm{d}\bar{T}/\mathrm{d}z$. Figure 4 shows the evolution of turbulent kinetic energy, KE, and turbulent potential energy, PE, for all the cases. These quantities are

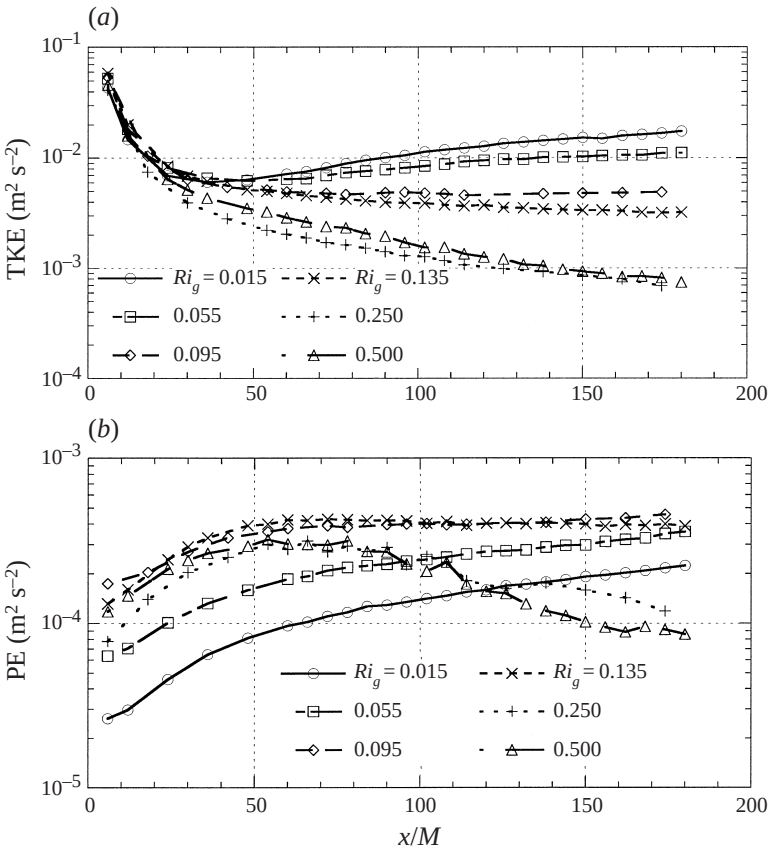

FIGURE 4. Evolution of turbulent kinetic and potential energies for all the cases. (*a*) Evolution of turbulent kinetic energy; (*b*) evolution of turbulent potential energy.

defined as

$$\mathrm{KE} = \tfrac{1}{2}(\overline{u^2} + \overline{v^2} + \overline{w^2}), \tag{3.1}$$

$$\approx \tfrac{1}{2}(2\overline{u^2} + \overline{w^2}), \tag{3.2}$$

$$\mathrm{PE} = \tfrac{1}{2}N^2 L_t^2, \tag{3.3}$$

where an approximation for KE is used, given only u, and w are available. $L_t = (\overline{\theta^2}/S_T^2)^{1/2}$ is the overturn scale. The equation for potential energy is a linearized version that is exact for linear internal waves (Holliday & McIntyre 1981). The evolution equations for these quantities can be found in Rohr *et al.* (1988), Holt *et al.* (1992), Jacobitz *et al.* (1997), and Piccirillo & Van Atta (1997), as well as others. As is shown in all of these references, for $Ri_g < Ri_{cr}$, where Ri_{cr} is a critical gradient Richardson number, the turbulent energies grow with evolution because net production is greater than both dissipation and buoyancy losses. For $Ri_g > Ri_{cr}$, the turbulence decays, presumably until some collapse of turbulence results in a new state of the turbulence. As shown in Keller (1999), the ratio KE/PE achieves a constant value, indicating either both quantities grow or both decay. As the turbulent energies grow, Re_λ also grows, whereas if the turbulence decays, Re_λ also decays.

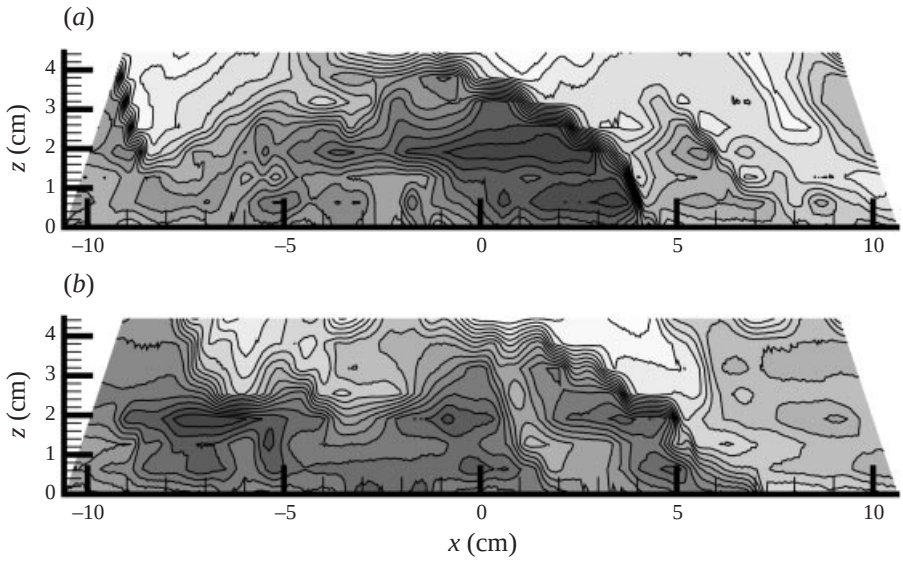

FIGURE 5. Two different isocontour plots of temperature at $x/M = 150$ for $Ri_g = 0.015$. Note the large temperature gradient regions aligned along the mean strain direction. The steps in the gradients are due to the limited resolution of the rake. Dark colouring indicates cool fluid, light colouring indicates warm fluid.

3.2. *Rake visualizations*

Isocontour plots of the temperature field from the rake measurements are used to visualize the temperature field. The plots are made with physically accurate proportions in which spatial coordinates are found by using a frozen flow approximation to convert from time steps to spatial steps using the local mean velocity. Starting from the middle of the time series, defined as $x = 0$, spatial increments are defined both forward and backward so the distortion occurs in both directions. The edges of the plots provide a measure of the total distortion, as indicated by the slope of the edge of the plot. The flow direction is from negative to positive x, and the flow velocity is highest at the bottom. Shading is used to label warm and cold fluid, where dark is cool and light is warm. The steps in the isocontours, often visible along high-gradient regions, are due to the limited resolution of the cold-wire rake, which has just eight points. Two different examples are shown for each of three cases, $Ri_g = 0.015, 0.095$, and 0.5.

$Ri_g = 0.015$

Figure 5 shows isocontours for $Ri_g = 0.015$ at $x/M = 150$ for two different examples. These figures show the typical structures found in flows where $Ri_g < Ri_{cr}$. Strong, stable gradient regions, which are long (at least 4 cm in these cases) are the strongest gradients in the flow. These are the microfronts discussed by Gerz & Schumann (1996). An examination of the plots indicates that these fronts are associated with parcels of fluid which were recently advected away from their neutral positions. As shown in these figures, large parcels of fluid which are cooler than the ambient have high-gradient regions to their right, or downstream, and large parcels which are warmer than the surrounding fluid have high-gradient regions on their upstream side.

This phenomenology is similar to that described in Tavoularis & Corrsin (1981*a*)

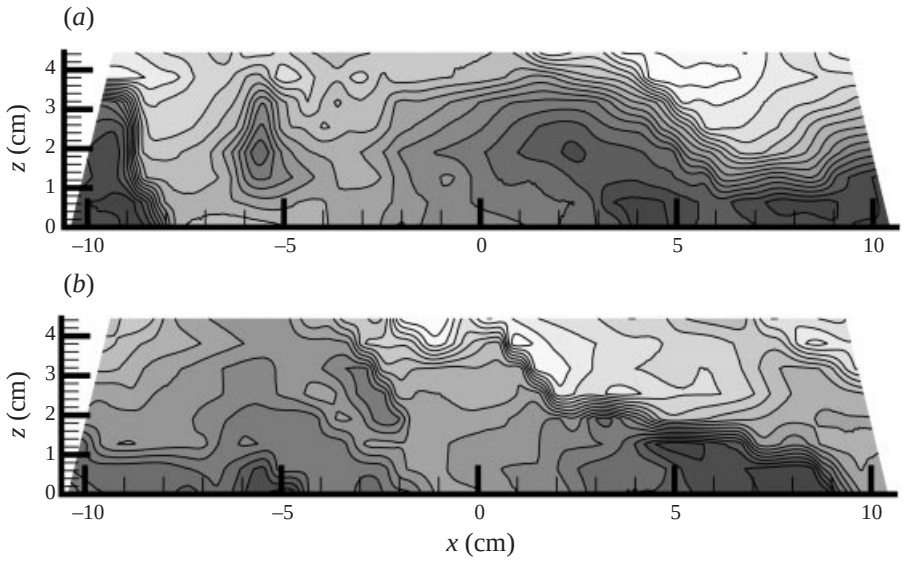

FIGURE 6. Two isocontour plots of temperature at $x/M = 150$ for $Ri_g = 0.095$. Note the high-gradient regions tend to curve toward horizontal, and isothermal regions are just above or below these high-gradient regions. See figure 5 for additional information.

and later in Budwig, Tavoularis & Corrsin (1985) in which it is postulated that parcels that are advected upward carry excess momentum compared to the surrounding fluid, creating a convergence zone on the front of the lump which increases the existing temperature gradient. Similarly, parcels that are advected downward, away from their neutral position, should have a deficit in momentum relative to the surrounding fluid, creating a convergence zone on the upstream side of the parcel. A physically reasonable way to describe these structures would be as pulsed jets exhausting into a crossflow, such that, initially, the gradient would be aligned almost vertically, but, eventually, the high gradient region becomes turned toward horizontal and strained beyond recognition.

$Ri_g = 0.095$

Figure 6 shows isocontour plots for stronger stratification. The contours are similar to the less stratified case, but the angle of the high-gradient region is less vertical. As cold fluid is advected upward, kinetic energy is converted to potential energy, and the vertical momentum of the parcel decreases. This results in the high-gradient regions turning toward horizontal more quickly than in the less stratified case. Such a mechanism should therefore result in larger vertical gradients, since the turning toward horizontal happens before the gradient is too distorted and before diffusion has acted. Figure 6(*a*) appears to show this tendency, where the tip of the cool lump, at $x = -1.0$ cm, could be falling because of buoyant forces. Without velocity measurements, we cannot be sure of the exact dynamics.

$Ri_g = 0.5$

The isocontour plots for $Ri_g = 0.5$ (figure 7) are in sharp contrast to the other two cases. No high-gradient regions are evident, and few regions of static instability are visible. These images could be considered wavelike, based on the limited slope of the isopycnals and the lack of unstable regions. To conclude that this is really waves

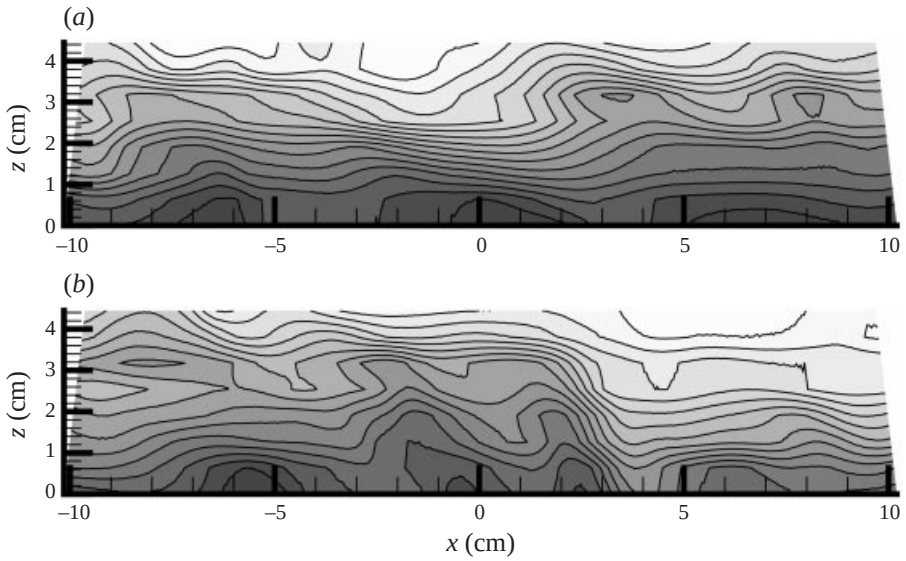

FIGURE 7. Two isocontour temperature plots at $x/M = 150$ for $Ri_g = 0.5$. The contours are distinctly wavelike, but with some overturned regions. See figure 5 for additional information.

would require measurements in both space and time to be able to track the motion of a line of constant phase. For waves in which the frequency is no greater than N, or period of $2\pi/N$, waves in this flow will have only propagated at most half a wavelength, since the travel time in the tunnel is about 2 s. No evidence of waves is found from single-point measurements of the cross-spectrum between vertical velocity and temperature. In this case, the phase spectrum between these two variables would be $\pm 90°$.

3.3. *Two-dimensional autocorrelations*

The visualizations discussed in the previous section are helpful for obtaining an understanding of the physical mechanisms, but a more quantitative result is preferred. Toward this end, two-dimensional autocorrelations of temperature have been calculated. The autocorrelation of temperature fluctuations is shown in figure 8(a, c, e) for three cases at the final streamwise station. Note that the limited vertical resolution causes some bumps in the curves. For $Ri_g = 0.015$, the isocontours strongly resemble the results in Tavoularis & Corrsin (1981*a*) for passively stratified shear flow. They found an angle of inclination of the major axis of a fitted ellipse to be about 25°. The angle of the contours in figure 8(a) is estimated to be about 35°, similar to the reported angle of inclined coherent horseshoe vortices (Gerz *et al.* 1994). Increasing stratification limits the vertical scales, causing the major axis to incline at smaller angles, as seen in these autocorrelation plots. At $Ri_g = 0.095$, the angle is about 31°. For $Ri_g = 0.5$, the angle is about 20°.

A measure of the structure of high-gradient regions is the autocorrelation of the streamwise gradients, shown in figure 8(b, d, f). Owing to the limited vertical resolution of the rake, vertical gradients cannot be measured, but, as is evident in the isocontour plots, high vertical gradients are probably highly correlated with high streamwise gradients. The streamwise gradients are calculated using 6th-order finite differences. For $Ri_g = 0.015$, the autocorrelation of the streamwise gradient shows that large streamwise gradients occur on a vertically aligned front for small vertical

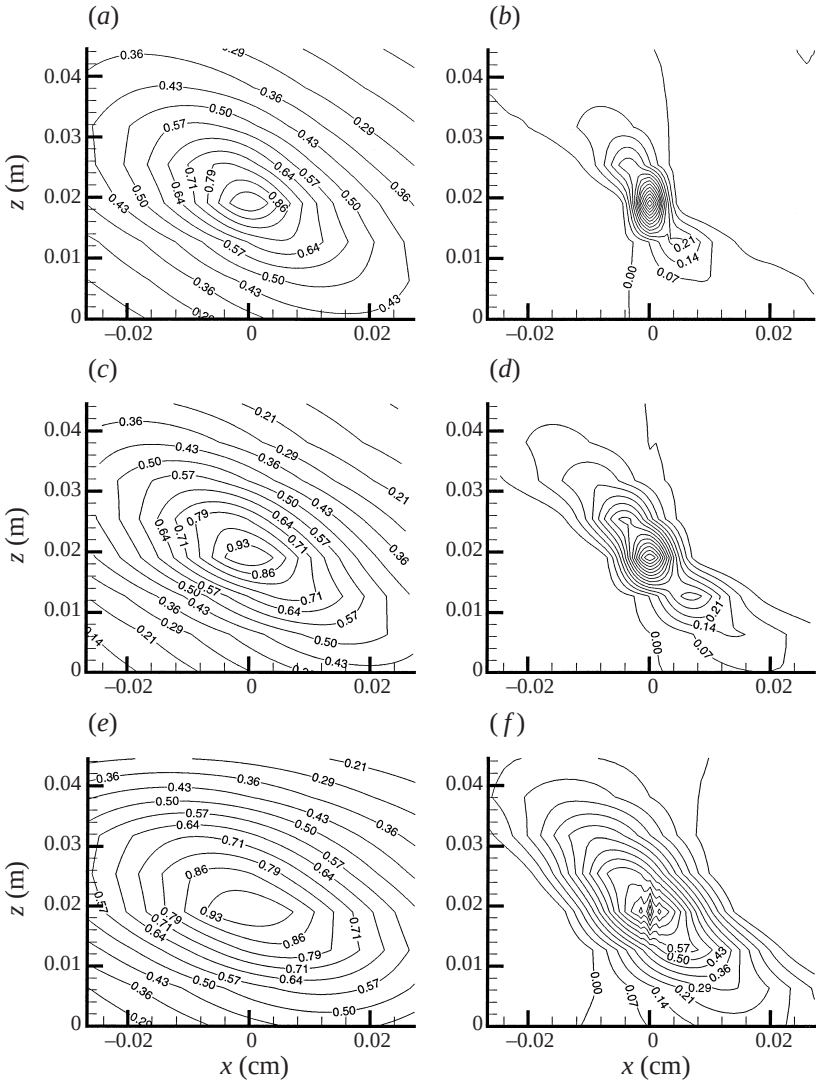

FIGURE 8. Isocontours of the autocorrelations of temperature fluctuations and of streamwise temperature gradients at $x/M = 180$. Isocontours, with contour labels, are plotted for values from 0 to 1. (a, c, e) Autocorrelation of temperature fluctuations for $Ri_g = 0.015, 0.095, 0.5$, respectively; (b, d, f) autocorrelation of streamwise gradients for $Ri_g = 0.015, 0.095, 0.5$, respectively.

scales. This structure is due to the short timescale of vertical advection relative to the shear timescale which results in the formation of large horizontal gradients before significant lateral advection has occurred. This description is consistent with the mechanism described in Tavoularis & Corrsin (1981*a*) and Budwig *et al.* (1985). With increasing stratification, vertical advection is inhibited by buoyancy, slowing down vertical advection. As the differential velocity has time to act, high-gradient regions are advected foward or backward and turned relative to the initial event. This aligns the gradients with the mean strain direction, at 45°. The difference in alignment of the gradients compared to the fluctuations implies that the structure of the gradient field is dependent on the mean strain field. This observation can be contrasted to the

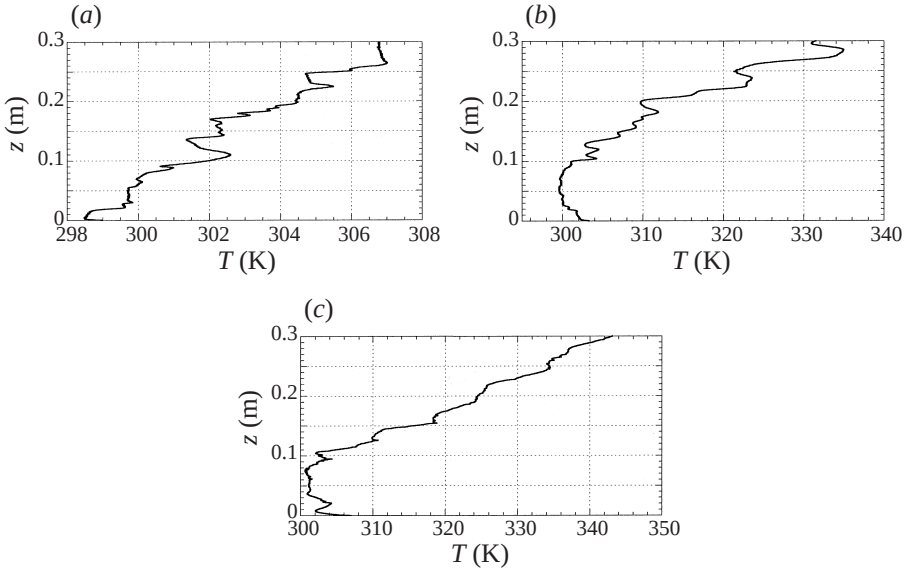

FIGURE 9. Examples of vertical profiles for three different cases of Ri_g. Primary features include large stable gradients, weak unstable gradients, and isothermal regions. Note the change of temperature scales and different mean temperature gradients. (*a*) $Ri_g = 0.015$, $\mathrm{d}\bar{T}/\mathrm{d}z = 38\,\mathrm{k\,m^{-1}}$; (*b*) $Ri_g = 0.095$, $\mathrm{d}\bar{T}/\mathrm{d}z = 163\,\mathrm{k\,m^{-1}}$; (*c*) $Ri_g = 0.5$, $\mathrm{d}\bar{T}/\mathrm{d}z = 224\,\mathrm{k\,m^{-1}}$.

study by Gerz & Schumann (1996) who theorize that the large gradients should lie parallel to the horseshoe vortices, at 35°. The differences in the results could be due to different flow conditions.

3.4. *Vertical temperature profiles*

Vertical temperature profiles for one station are shown for $Ri_g = 0.015$, 0.135, and 0.5 in figure 9. An examination of these profiles shows regions of static instability and regions of high stable gradient. The large stable gradients are greater in magnitude than the unstable gradients and correspond to the large gradients visible in the rake measurements above. Typically, just above or below the stable gradient is a region of roughly constant temperature, over a scale of 1 cm. These regions correspond to the advected parcels visible in the rake measurements.

A diagram of how the vertical profiles correspond to the overall structure found in the rake measurements is shown in figure 10 for a cool parcel advected upward. As illustrated in the figure, stable gradients, uniform temperature lumps, and unstable regions are all direct results of vertical advection events. The direction of the advection determines where, relative to the advected parcel, the high-gradient region and the unstable region occur. For a cold parcel advected upward, the high stable gradient region is on the upper edge of the parcel and the unstable region is on the opposite side of the parcel. A warm parcel advected downward has the opposite orientation.

The generation of large vertical gradients produces a skewness of the vertical fluctuating temperature gradient of about 1.1, consistent for all the cases. This skewness is evident in the probability density function (PDF) of the fluctuating vertical temperature gradient shown in figure 11, where

$$\alpha\left(\frac{\partial\theta}{\partial z}\right) = \frac{(\partial\theta/\partial z) - (\overline{\partial\theta}/\partial z)}{\left(\partial\theta/\partial z\right)'}. \tag{3.4}$$

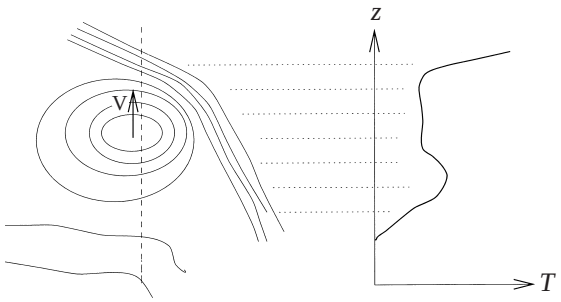

FIGURE 10. Schematic of how vertically advected parcels at large scales create high gradients and unstable regions in a mean flow with $d\bar{U}/dz < 0$ and flow from left to right. A vertically advected lump is pushed back over warmer fluid by the mean velocity gradient as a convergence zone forms on the downstream side of the parcel because of the excess momentum carried by the parcel relative to the fluid around it. For downwardly advected parcels, the same mechanism results in a convergence zone on the upstream side of the lump and a reversed temperature profile.

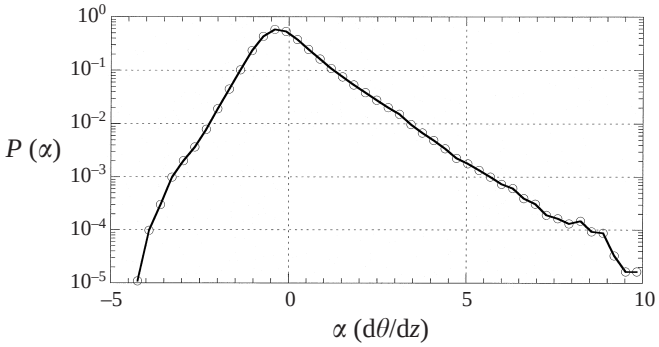

FIGURE 11. PDF of the fluctuating vertical temperature gradient. The asymmetry of the curve indicates a positive skewness. This curve is typical for all the cases and streamwise stations. $x/M = 30$; $Ri_g = 0.015$.

The asymmetry of the PDF implies a positive skewness. Note the exponential tails of the PDF. Thoroddsen (1991) reports skewness measures of the vertical temperature gradient which are initially about 1.0, but decay to about 0.4. The larger values found in the present study for sheared stratified turbulence are probably due to the presence of shear. Similar to Thoroddsen, the PDF of θ is Gaussian.

3.5. *Vertical wavenumber spectra and mean-square gradients*

Vertical wavenumber spectra are calculated from the vertical profiles by computing a spectrum for each profile and averaging over all profiles at a station. The spectrum for each profile is calculated relative to a linear least-squares fit through the data. This method is used instead of the usual definition, as a fluctuation relative to the mean gradient, because it was found that significant energy was contained in vertical scales larger than the measurement length. By using a local reference, the large scales are effectively high-pass filtered without allowing the energy from these large scales to alias into the smaller scales. The present method does not change the small scales, but the integral scale based on this spectrum probably does not reflect the overall vertical integral scale. It is arguable, however, that this spectrum does reflect the largest turbulent scales.

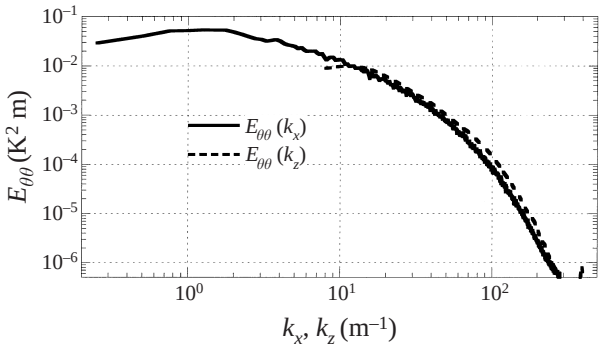

FIGURE 12. Horizontal and vertical wavenumber temperature spectra are compared at $x/M = 150$ for $Ri_g = 0.135$. This example was chosen to illustrate the differences in the spectra. The vertical wavenumber spectrum spans a narrower band of scales than the horizontal wavenumber spectrum, and therefore must have more energy at small scales.

The vertical wavenumber spectrum for one case at one station is compared to the local horizontal spectrum calculated from fixed-point measurements and using frozen-flow approximation in figure 12. The vertical wavenumber spectrum occupies a narrower range of scales than the horizontal, but has greater energy (since the two curves must integrate to the same amount of energy, this relationship is expected). At the small scales, the curves meet, indicating the very smallest scales are approximately isotropic in energy.

The evolution of the vertical wavenumber spectra is very similar to that found in horizontal spectra (see Rohr *et al.* 1988 or Piccirillo & Van Atta 1997). Spectral evolution for three cases, $Ri_g = 0.015, 0.095, 0.5$ is shown in figure 13. For low Ri_g, the energy in the large scales increases, resulting in a slow increase in energy in the small scales. At high Ri_g, the energy in the large scales decays continuously, and therefore, without a source of energy, the small scales decay.

To study the total small-scale anisotropy, the ratio of the vertical mean square fluctuating temperature gradient to the streamwise mean square fluctuating temperature gradient is plotted in figure 14. The curves are separated into two cases, corresponding to low or high Ri_g. In figure 14(*a*), the ratio is plotted against $\tau_S = \int_0^x (S(x')/U(x'))\mathrm{d}x'$, a non-dimensionalized time. The ratio, $r = \overline{(\partial\theta/\partial z)^2}/\overline{(\partial\theta/\partial x)^2}$, begins near a value of 1.0, grows to a maximum of around 2.0, at $\tau_S \approx 8$, and subsequently decays. In contrast, figure 14(*b*) shows r for the most stratified cases, plotted against $\tau_N = \int_0^x (N(x')/U(x'))\mathrm{d}x'$. For these cases, r also begins near 1.0, but grows continuously, reaching values of about 3.0. The results can be compared to the measurements of r in Thoroddsen & Van Atta (1996) in unsheared, stratified turbulence using two-point methods. Thoroddsen & Van Atta found a continuous increase in r, as in figure 14(*b*), but their magnitude of r is only about 2.0 for similar evolution times.

3.6. *Thorpe scales*

A quantification of the size of unstable regions is made possible using Thorpe sorting, and calculating Thorpe scales (see Dillon 1982). A Thorpe displacement is defined relative to a stable profile, which in this case is defined as the profile found by sorting the instantaneous temperature profile. According to Dillon, this is the profile which would result if the temperature field was allowed to adiabatically settle back to a stable profile. The stable profile is found by a bubble sort method. The displacement, δ, is the distance a parcel must be moved to obtain the stable profile. One example of

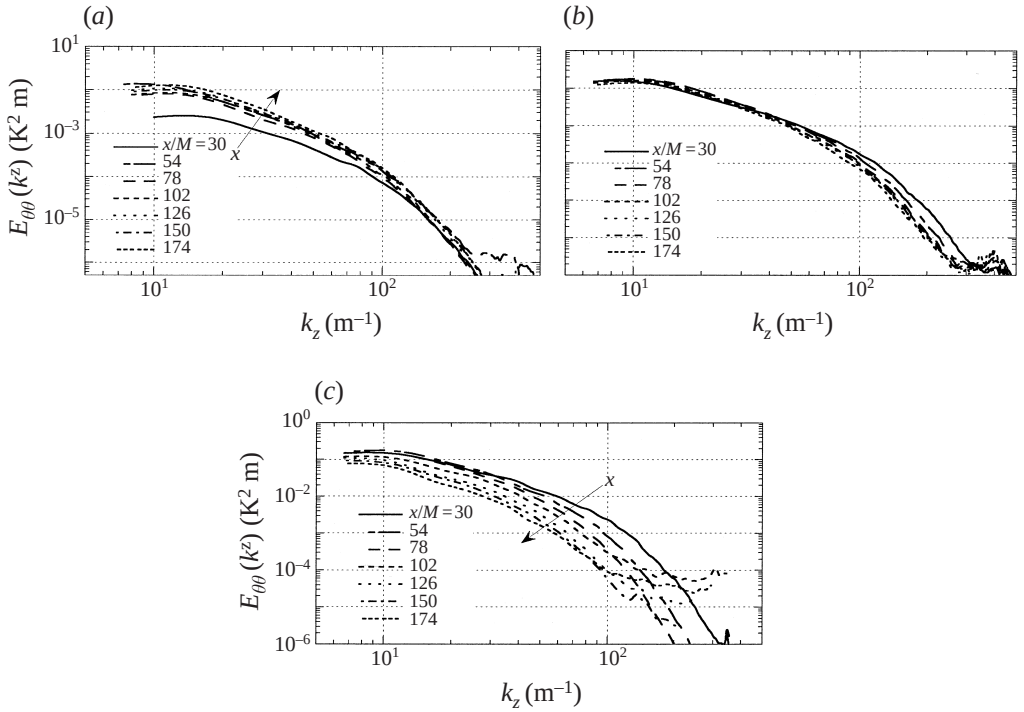

FIGURE 13. Spectral evolution for three different cases of Ri_g. As in the case of horizontal wavenumber spectra, at low Ri_g, energy increases in large scales and small scales. For large Ri_g, energy decreases in large scales, which accelerates decay of energy in small scales. (*a*) $Ri_g = 0.015$; (*b*) $Ri_g = 0.095$; (*c*) $Ri_g = 0.5$.

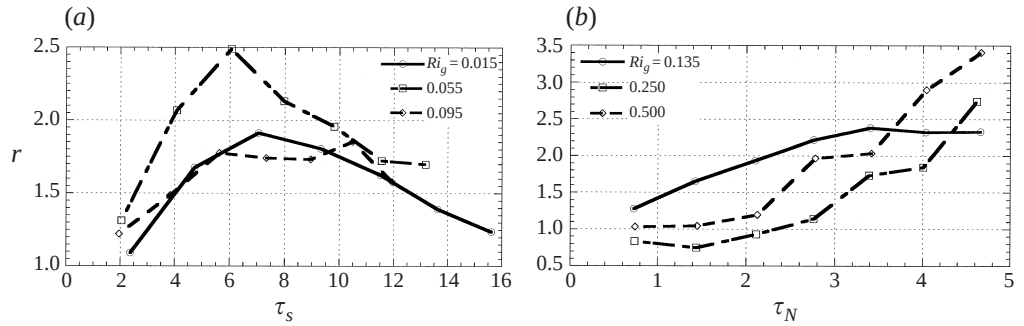

FIGURE 14. The ratio r is plotted for all the cases. To emphasize the different controlling properties, the plots are split into low Ri_g, using 'St' scaling, and high Ri_g using 'Nt' scaling. (*a*) low Ri_g; (*b*) high Ri_g.

a vertical profile, its sorted profile, and the resulting Thorpe displacements is shown in figure 15.

The Thorpe scale, L_{Th}, is calculated as the root mean square displacement over all N profiles and M_i non-zero displacements in each profile,

$$L_{Th} = \left[\frac{1}{N} \sum_{i=1}^{N} \frac{1}{M_i} \sum_{j=1}^{M_i} \delta_j^2 \right]^{1/2} . \tag{3.5}$$

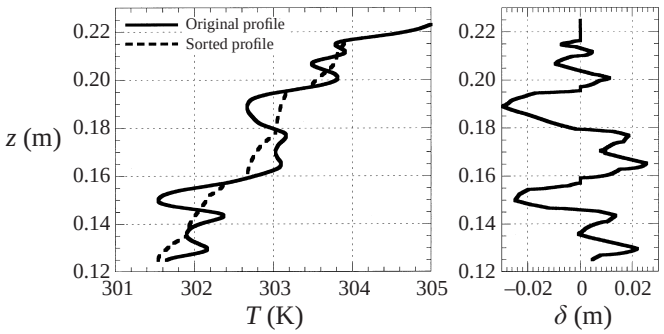

FIGURE 15. Example of Thorpe sorting and the resulting Thorpe displacements, δ.

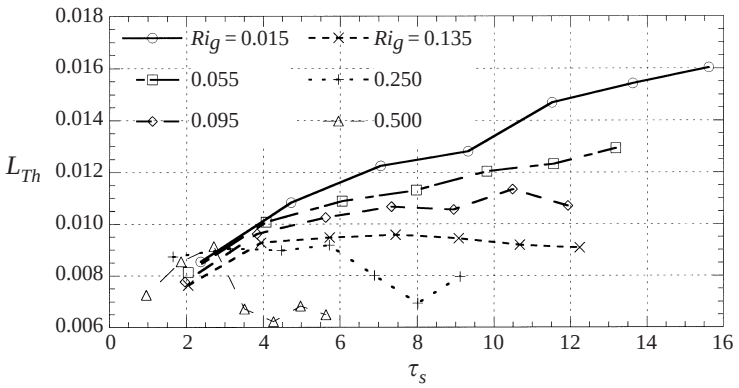

FIGURE 16. Evolution of the L_{Th} for all cases. The partial collapse as a function of St implies the initial growth is controlled by shear.

This definition is different from previous definitions, especially compared to that of Itsweire (1984) and Itsweire *et al.* (1993), in which L_{Th} is calculated as a vertical average over all values, even zero values. As we are interested in the size of unstable regions, we do not average over zero displacements, since those are by definition regions of stability. L_{Th} is thus a measure of the size of unstable regions only. In contrast, the Thorpe scale defined by Itsweire *et al.* is a measure of the average length of instability over the whole vertical profile.

Figure 16 shows the evolution of L_{Th} for each case. For early evolution times, the growth of L_{Th} is approximately the same for all cases. A visible collapse of the curves indicates that shear effects control this initial growth. For further evolution times at low Ri_g, L_{Th} increases throughout the evolution, indicating that the size of unstable regions continues to increase. For increasing stability, the rate of growth is less. For the most stable cases, $Ri_g = 0.25, 0.5$, the lengthscale initially increases to maximum, decays slightly, but then remains roughly constant. Further evolution time in the most stratified cases might show a final decay in L_{Th}, when overturns cease to exist, but that cannot be evaluated here.

L_{Th} is compared to the overturn scale, $L_t = (\overline{\theta^2}/S_T^2)^{1/2}$ in a similar manner to Itsweire *et al.*, by plotting L_{Th} versus L_t in figure 17(*a*). For low Ri_g, the points generally line up parallel to the reference line (with slope equal to one). As Ri_g

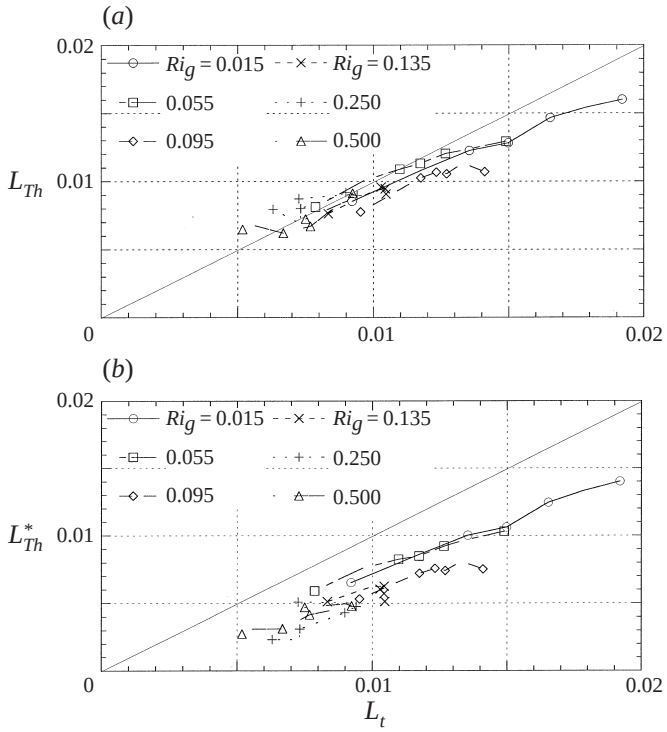

FIGURE 17. A comparison of L_{Th}, L^*_{Th}, and L_t. The straight line through both plots has slope equal to 1. (*a*) L_{Th} versus L_t; (*b*) L^*_{Th} versus L_t (similar to Itsweire *et al.*). In (*b*), L^*_{Th} is approximately proportional to L_t for all the data, whereas in (*a*), the L_{Th} increases relative to L_t for smaller values of L_t.

increases, and with flow evolution, L_t decays relative to L_{Th} such that the overall curve crosses the reference line, indicating that the average isopycnal displacement is decaying faster than the scale of the overturns. To compare our results to those of Itsweire *et al.*, we have also plotted L^*_{Th}, a Thorpe scale computed by averaging over all displacements, versus L_t, in figure 17(*b*). This plot is similar to their figure 2, showing an approximate constant proportionality between L^*_{Th} and L_t. It does not show an eventual decay of L^*_{Th} relative to L_t.

Taking figures 16 and 17 together, a physical interpretation of these results is that even though the total energy of the field is decaying, the size of unstable regions is not decaying as quickly. Therefore, even though the overturns are not becoming smaller, there are fewer and fewer overturns. This is supported by the results below for available potential energy.

The probability density function (PDF) of Thorpe displacements is shown in figure 18. The figure shows obvious exponential tails, and implies that the Thorpe scale can be interpreted as a measure of the slope of the tails. This result can be compared to PDFs of temperature, since the instantaneous temperature is directly dependent on these displacements. The statistics of θ can range from Gaussian to non-Gaussian depending on the microscale Reynolds number of the turbulence and size of the domain relative to the integral lengthscale (Warhaft 2000). The difference between fluctuations defined around the local stable profile and fluctuations defined around the mean are investigated by a new decomposition which uses the local background

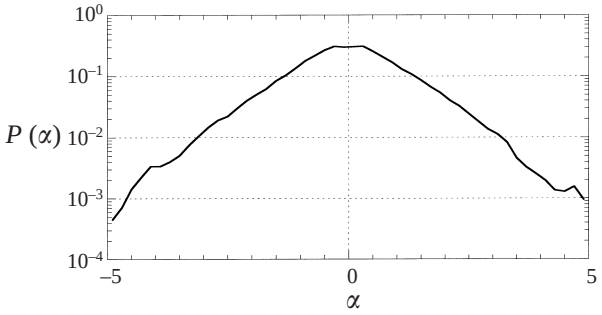

FIGURE 18. PDF of Thorpe displacements at $x/M = 30$, $Ri_g = 0.015$. Exponential tails of the PDF indicate the Thorpe scale is a measure of the slope of the tails.

temperature profile, T_b. The decomposition is as follows:

$$\theta = T - \bar{T}, \tag{3.6}$$

$$\theta_1 = T - T_b, \tag{3.7}$$

$$\theta_2 = T_b - \bar{T}, \tag{3.8}$$

$$\theta = \theta_1 + \theta_2. \tag{3.9}$$

Thus, θ, defined relative to the mean, is split into a part associated with the Thorpe displacement, θ_1, and a part associated with stable fluctuations, θ_2. The contributions to $\overline{\theta^2}$ by θ_1 and θ_2 are shown in figure 19 where it is obvious that most of the energy in θ is contained in stable fluctuations associated with the background density profile. This result implies then that overturn scales, defined as $L_t = (\overline{\theta^2}/S_T^2)^{1/2}$, are primarily a measure of the height of stable displacements of isopycnals. θ_1 is directly related to the Thorpe displacement. That the correlation between θ_1 and θ_2 is low (the normalized correlation is about 0.1) implies that Thorpe scales and overturn scales are not strongly related. These results hold for all of the cases studied here. The probability density functions of θ, θ_1 and θ_2 are shown in figure 20. In sharp contrast, the PDF of θ_1 has exponential tails, whereas the PDF of θ and θ_2 are Gaussian. Since the contribution to $\overline{\theta^2}$ is primarily due to θ_2, the Gaussian PDF of θ is the same as the PDF of θ_2. The difference in these PDFs is similar to the result found in Christie & Domaradzki (1994) for thermal turbulence where the fluctuations associated with large scales were Gaussian but fluctuations associated with small scales were exponential. In this case, it might be interpreted that the stable fluctuations are wavelike, and therefore are associated with larger scales.

3.7. *Available potential energy*

The available potential energy per unit mass is defined as

$$\mathrm{APE} = \frac{1}{\rho_o l} \int_0^l g(\rho(z) - \rho_*(z)) z \mathrm{d}z \tag{3.10}$$

which can be found in Dillon (1984), Winters *et al.* (1995), and others. ρ_o is the average density over the interval of length l and $\rho_*(z)$ is the sorted density profile as defined above. Temperature is converted to density using the perfect gas law. The mean APE is found as the average value of (3.10) over all the vertical profiles. The evolution of the ratio of APE to the background potential energy $P_b = (1/\rho_o l) \int_0^l g\rho_*(z) z \mathrm{d}z$ is

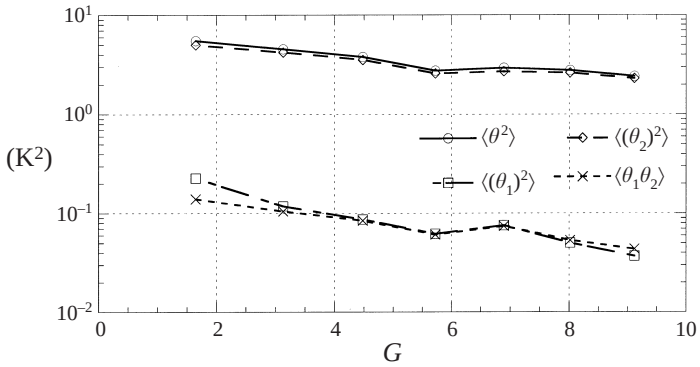

FIGURE 19. The contributions to θ are compared for $Ri_g = 0.015$. $\overline{\theta^2}$ is comprised primarily of contributions from θ_2. $\langle()\rangle$ indicates a mean quantity.

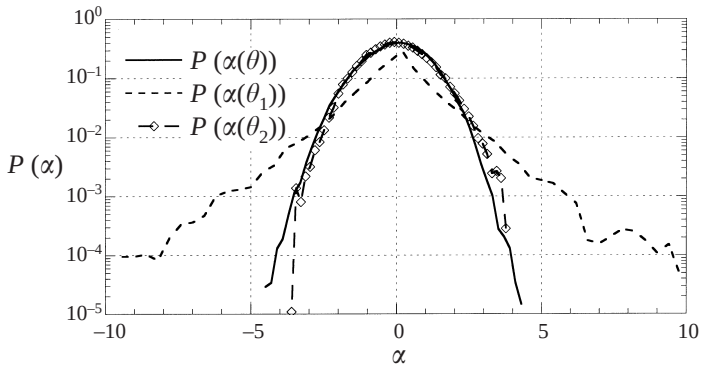

FIGURE 20. PDFs of θ, θ_1 and θ_2 at $x/M = 30$, $Ri_g = 0.015$. The PDFs for θ and θ_2 are very close to Gaussian, whereas the PDF for θ_1 has strongly exponential tails.

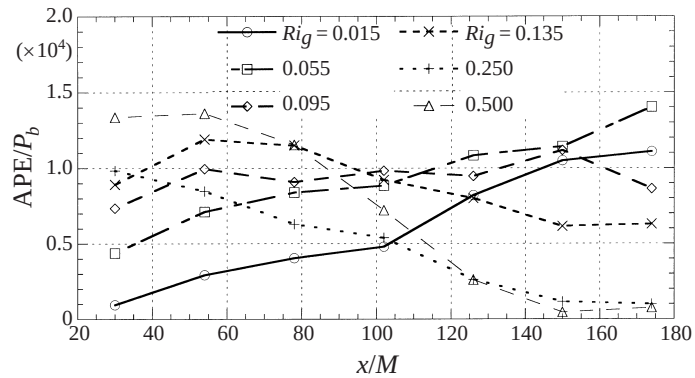

FIGURE 21. Ratio of APE to P_b for all cases. P_b changes very little through evolution, so these curves represent primarily the evolution of APE.

shown in figure 21 which shows that the APE $\ll P_b$ and that APE grows and decays according to the stability based on Ri_g.

The ratios APE/KE and APE/PE are shown in figure 22. The absolute magnitude of APE depends on the length of the integral, l, since the integral is nonlinear in

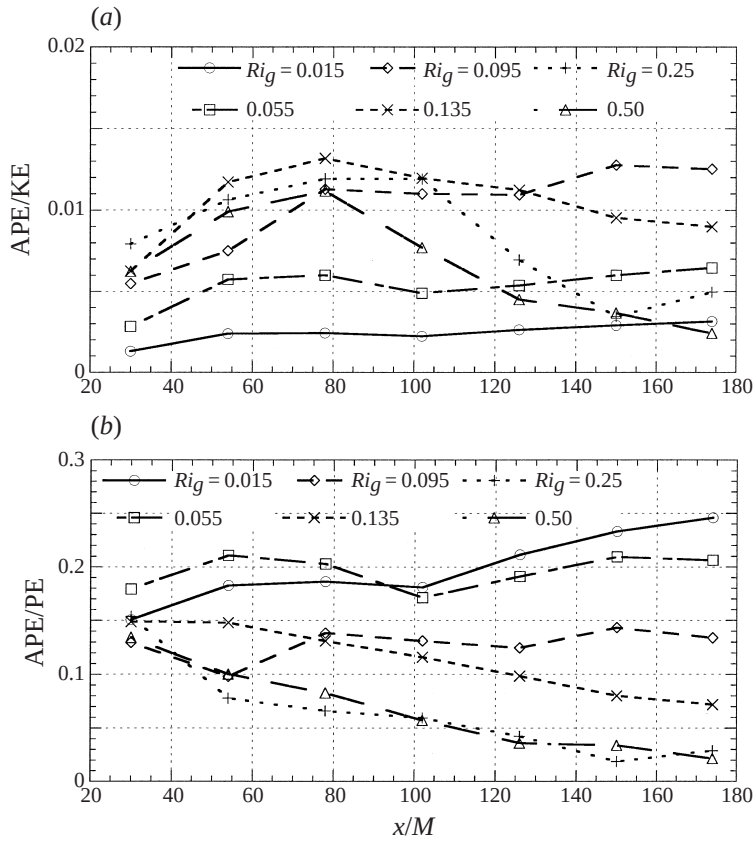

FIGURE 22. Ratio of APE to KE and PE. For low Ri_g, APE increases relative to both KE and PE, indicating more energy is associated with overturn regions. For high Ri_g, APE decays toward zero relative to KE and PE, indicating fewer overturns are occurring.

z. To ensure the ratios for different cases are comparable, the integration length for every measurement is 10 cm. Compared to KE, APE always increases initially, but subsequent evolution depends on Ri_g, where for low Ri_g, the ratio continues to grow, but for high Ri_g the ratio can fall quickly. The ratio APE evolves monotonically in every case, where the ratio increases for low Ri_g but decays for high Ri_g. These results show that the proportion of energy associated with unstable regions varies relative to both the kinetic energy and the potential energy. In some sense, these energies can be considered independent types of energy. The result implies the approximation used by Dillon (1984) to equate PE with APE is not correct, since the two quantities evolve at different rates and, in this study, APE $\ll$ PE.

3.8. *Diapycnal flux*

The diapycnal flux is defined by Winters *et al.* (1995) as the flux across isopycnal surfaces which results in irreversible mixing. This irreversible mixing increases the background potential energy, defined as the minimum potential energy which a volume can take by adiabatic reordering. The change in background potential energy is best understood as the difference in potential energy of a volume before mixing begins and after mixing has totally died away. Winters *et al.* show that the instantaneous

diapycnal flux of buoyancy per unit mass, ϕ_d, can be written as

$$\phi_d = \kappa \frac{g}{\bar{T}_o} \frac{|\nabla T|^2}{(\mathrm{d}T/\mathrm{d}z_*)}, \tag{3.11}$$

where some constants are used to convert a diapycnal flux of T to a flux of buoyancy per unit mass. $\mathrm{d}T/\mathrm{d}z_*$ is the local gradient of the sorted, stable profile and $|\nabla T|^2$ is the total squared temperature gradient. As discussed by Winters & D'Asaro (1996) and Winters *et al.* (1995), the diapycnal flux is the molecular mixing across isopycnal surfaces. This flux is across surfaces which are contorted, thereby increasing the effective amount of surface across which diffusion occurs. A fundamental role of turbulence is to both create more surface area and to create local high-gradient regions. Both of these mechanisms enhance the rate of molecular mixing as compared to the diffusion by molecular mixing of the mean gradient. For the present flow conditions, where the flow is homogenous in the y and z directions, an equation relating average buoyancy flux, diapycnal flux and available potential energy can be derived from equation (19) in Winters *et al.* (1995). By taking the expectation of that equation, and noting that the flux in homogeneous directions is equal into and out of the volume, the equation for the evolution of available potential energy can be reduced to:

$$U \frac{\mathrm{dAPE}}{\mathrm{d}x} = B - \phi_d + \phi_i, \tag{3.12}$$

$$\frac{U}{B} \frac{\mathrm{dAPE}}{\mathrm{d}x} = 1 - \frac{(\phi_d - \phi_i)}{B}, \tag{3.13}$$

where all the terms are average quantities and $\phi_i = (g/\bar{T}_o)\kappa S_T$ is the mean molecular flux of buoyancy. Non-dimensionalizing the equation with the buoyancy flux, it is seen that the ratio $(\phi_d - \phi_i)/B$ determines whether or not APE grows or decays. Since ϕ_d incorporates the mean molecular flux, the difference $\phi_d - \phi_i$ is the effective rate at which APE decreases owing to molecular mixing.

The diapycnal flux can be estimated from the vertical profiles of temperature using the vertical density gradients and sorted profiles of density along a line measurement. The original formulation of Winters *et al.* (1995) assumes that the background density gradient is based on a reordering of a volume, instead of a line. It is not clear what effect this difference has on the results. ϕ_d is calculated by computing (3.11) in each profile at each point by calculating local density gradients using 6th-order finite differences on both the original profile and the sorted profile. The quantity $(\partial T/\partial z)^2/\mathrm{d}T/\mathrm{d}z_*$ is averaged over all points in the central 10 cm of the flow and averaged over all of the profiles. An equivalent average can be obtained by averaging over isotemperature values in the core of the flow over all the profiles and then averaging over a range of temperatures in the homogeneous core, following the scheme outlined in Winters & D'Asaro (1996). As all the components of the gradient of temperature are not available, the flux is corrected using the measured ratio of the streamwise and vertical mean square fluctuating temperature gradients. The spanwise (y-direction) mean square fluctuating temperature gradient is estimated as the average between the streamwise and the vertical mean square gradients. The form of this correction can be found in the Appendix.

A plot of the ratio $(\phi_d - \phi_i)/B$ versus streamwise distance is shown in figure 23. For all of the cases, $(\phi_d - \phi_i)/B > 1$, indicating APE should decay for all cases, which does not match up with figure 21 which shows APE growing for $Ri_g \leqslant 0.095$. It is not clear that the growth rates of APE (positive and negative) do not match with

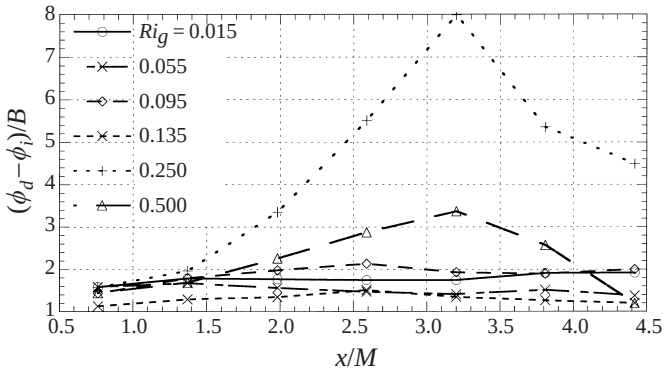

FIGURE 23. The ratio of diapycnal flux minus mean molecular flux to buoyancy flux. For most cases, the ratio is about 1.5 through the evolution. For $Ri_g = 0.25, 0.5$, the ratio is much larger, and evolves to a maximum before decaying.

the expected growth rates from the calculation of $(\phi_d - \phi_i)/B$. One possible reason is that defining the stable density profile by reordering a line measurement may not be exactly equivalent to the stable density profile obtained by reordering a volume. Also, it was found that the instantaneous value of ϕ_d at a point was very intermittent owing to the occasional small value of the stable gradient in the denominator, producing spikes in the data.

Considering figure 23 alone, the results show that the ratio is greatest for $Ri_g \geqslant 0.25$. For $Ri_g = 0.25, 0.5$, the flux ratio initially grows to a maximum and then decays and the ratio is greatest for $Ri_g = 0.25$. For $Ri_g \leqslant 0.25$, the flux ratio is almost constant throughout the evolution, with some scatter in the data. The strong increase in the flux ratio for $Ri_g = 0.25, 0.5$ illustrates how, for these cases, the buoyancy flux collapses at a faster rate than diapycnal flux. Therefore, when buoyancy flux has decayed to a negligible value, diapycnal flux can still persist, by acting on the almost fossilized temperature structure, thereby changing the background potential energy. In other words, in the absence of buoyancy flux, diapycnal mixing still occurs because the temperature structure still contains high-gradient regions and convoluted surfaces which enable molecular mixing to occur at a greater rate than the mean molecular mixing rate.

The diapycnal flux is also compared to the mean molecular flux in the form of a Cox number, where $Co_d = \phi_d/((g/\bar{T}_o)\kappa S_T)$. The evolution of Co_d is shown in figure 24. As expected for these types of flow, Co_d increases from 8 to 20 for the least stratified case. As stratification is increased, Co_d grows less strongly. For $Ri_g \geqslant 0.135$, the Co_d decays throughout the evolution. For the most stratified case, $Ri_g = 0.5$, Co_d decays to a value just larger than 1, indicating the flux at the last measurement station is mostly due to the mean molecular flux.

It makes sense that the flux ratio would have its greatest value at $Ri_g = 0.25$, which is similar to other results showing the flux Richardson number, $R_f = B/(B + \epsilon)$, having a maximum at $Ri_g = 0.25$ (Holt *et al.* 1992). For both the flux ratio in figure 23, and R_f, increasing the temperature gradient, for fixed mean shear rate, increases the buoyancy flux but also decreases the shear production of turbulent kinetic energy, which subsequently reduces the buoyancy flux. Thus, there is a competition between the kinematic effect due to increasing the temperature gradient and the dynamic effect of increasing the temperature gradient, which increases the stabilizing effects of gravity.

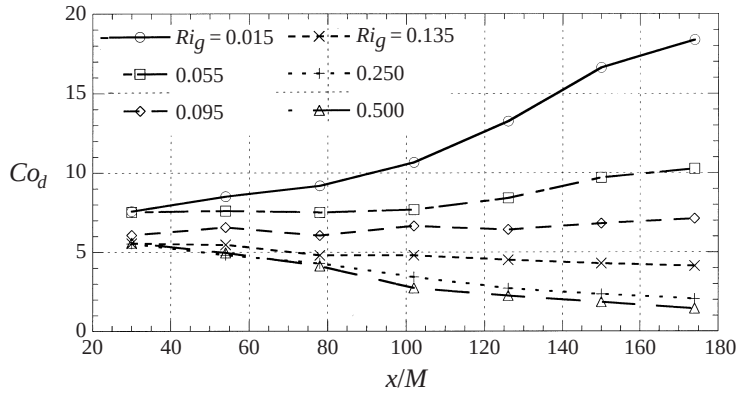

FIGURE 24. The evolution of Co_d for all the cases. The rapid rise of Co_d for low Ri_g is evidence for turbulent mixing increasing the effective diapycnal flux of buoyancy. For increasing stratification, Co_d decays toward a value of 1.0, showing that at the final stage, diapycnal flux is due primarily to mean molecular flux.

Staquet (2000) suggest that the flux Richardson number, usually defined as $R_f = B/(B+\epsilon)$, where B is the buoyancy flux and ϵ is the dissipation rate of kinetic energy, be defined instead as $R_f^* = (\phi_d - \phi_i)/(\phi_d - \phi_i + \epsilon)$. We compare the two definitions of R_f in figure 25. The shapes of the curves for the two definitions are very close, but R_f^* reaches higher values than R_f. R_f^* evolves to a value of about 0.5 for $Ri_g \geqslant 0.135$.

4. Discussion

4.1. *Shear distortion and creation of small vertical scales*

The ratio of the mean square fluctuating temperature gradients shown in figure 14(*a*) illustrates how for high shear rates relative to the reciprocal of the turbulent turnover time scale, small vertical scales are generated compared to horizontal. That the initial rise to a maximum in the ratio of mean square gradients is associated with shear is seen by similar evolution of the three cases for which each has a different shear rate. The maximum occurs at a non-dimensional evolution time of $\tau_S = 8$ which is approximately when self-similar, exponential evolution begins. Thus, the increase in energy at small vertical scales is a linear effect of distortion by mean vertical shear. Salmon (1998) illustrates this concept by solving for the evolution of mean square scalar gradients under the action of shear and molecular diffusivity. It is shown that the vertical shear transfers energy from large vertical scale to smaller vertical scales, while the energy in the horizontal scales is unaffected. This result is directly applicable to a turbulent field, and is one of the results from rapid distortion theory discussed in Hunt & Carruthers (1990). The subsequent decay of r for further evolution can be explained by the increasing intensity of mixing, such that the turbulent timescale is decreasing relative to the shear timescale. Therefore, turbulent mixing is redistributing the energy more efficiently before shear can effect the structure.

For high Ri_g, r increases continuously. The rate of this increase and the final values are significantly greater than that found for measurements in unsheared, stratified turbulence by Thoroddsen & Van Atta (1996). This increased rate of growth of r could be due to the combined effects of shear and stratification creating small-scale anisotropy. Since stratification effects damp out the turbulence shear production (Rohr *et al.* 1988), the shear only distorts the turbulence and does not promote its isotropy by

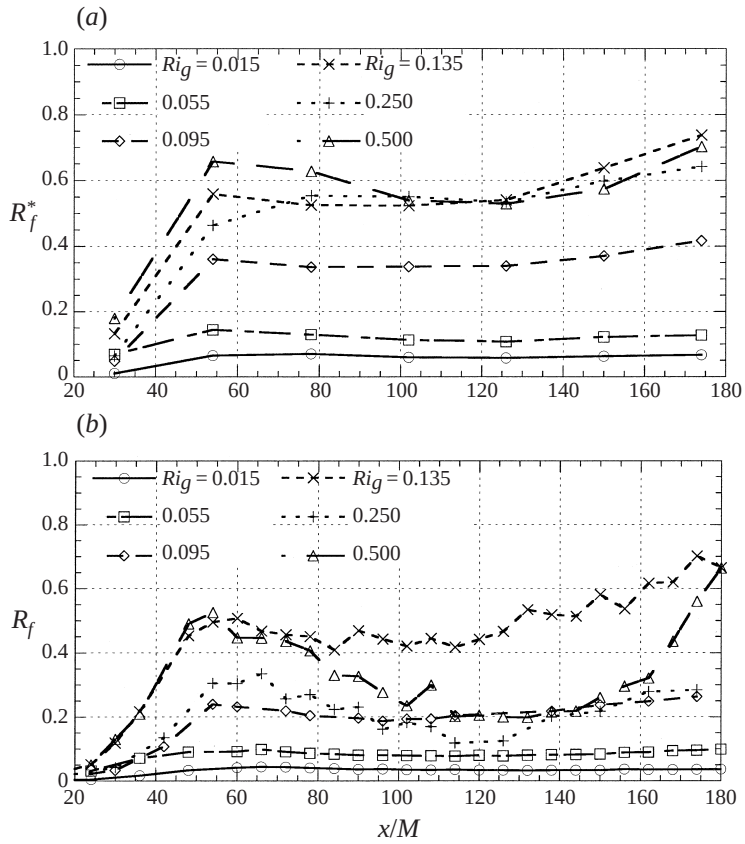

FIGURE 25. Two definitions of the flux Richardson number are compared. (*a*) R_f^* versus x/M; (*b*) R_f versus x/M. R_f^* shows a greater mixing efficiency than the buoyancy flux, but the overall shape is similar.

transferring energy into the turbulence. At the same time, high stratification increases the ratio by directly suppressing the vertical lengthscale of mixing.

4.2. *Waves versus turbulence*

The rake visualizations in figure 7 and the value of the Cox numbers in figure 24 for high Ri_g imply that the flow is wavelike. An additional factor which supports this conclusion is a measured negative Reynolds stress, implying a transfer of energy from KE to the mean flow. A conclusive measurement of waves cannot be made without time–space measurements in which a line of constant phase can be tracked through space. For this flow, the phase speeds are much less than the mean velocity, and therefore a wave is approximately frozen as it is measured. Furthermore, a wave which was emitted somewhere upstream in the flow probably cannot have even propagated through one phase, since the minimum period for a wave would be $2\pi/N$, which is about 3 s, compared to the travel time in this flow which is about 2 s. A more viable interpretation of the flow measured at these stations is as bobbing lumps of fluid which presumably emit internal waves. This type of phenomenology is similar to that described by Gerz, Schumann & Elghobashi (1989) and Komori *et al.* (1983) as bobbing fluid parcels, interspersed with both down gradient mixing events and counter-gradient restratification events. In terms of a fixed-point measurement,

a bobbing fluid element would be at a random stage in its evolution, possibly rising, falling, or perfectly still, when the fluid element was measured. In the context of the presently defined mean shear flow, in which $\mathrm{d}\bar{U}/\mathrm{d}z < 0$, a rising lump would have a positive velocity and a negative temperature fluctuation. The streamwise velocity fluctuation u is consistently measured to be negative for times when w is positive, or vice versa (i.e. $\overline{uw} < 0$). This implies that the lump is pushed slightly back relative to the local mean flow for rising lumps, or pushed forward for falling lumps. A possible reason for this is that a local pressure gradient develops owing to the convergence of density at the front of a rising lump or at the rear of a falling lump.

A picture of the flow can be constructed. Bobbing lumps rise up and down in the flow. For a large enough vertical rise, the lump can be pushed out over (under) fluid of lower (higher) density, thus creating a statically unstable patch. The vertical size of these patches is limited, as seen in the measurements of Thorpe scales. A possible mechanism for limiting this size is a viscous cutoff, similar to the cutoff for instabiliy of internal waves approaching a critical layer (see Baines 1995). In this case the bobbing lumps must be far enough from equilibrium for the local pressure gradients to act significantly in pushing the lumps forward or backward. For lumps that are not high (or low) enough, viscous effects keep overturns from occurring.

5. Conclusions

The vertical structure of the temperature field of homogeneous stratified shear turbulence has been studied using approximately instantaneous vertical profiles of temperature, supplemented with vertical rake measurements of temperature and standard fixed-point measurements of velocity and temperature. Vertical profiles contain unique information which is not available in standard fixed-point measurements. From the vertical profiles, measurements of Thorpe scales, available potential energy, and vertical wavenumber spectra were calculated and compared to other measured quantities.

It is found that the temperature structure of low Ri_g is strongly controlled by mean shear and the appearance of high-gradient regions generated by advective flux. Mean shear causes distortion of the vertical temperature structure to generate smaller vertical scales. Vertical advection generates both high stable gradients and local unstable regions. For high Ri_g, the temperature structure is modified primarily by the effects of stratification restraining vertical motions, but also by shear distortion. This enhances the development of small vertical scales which persist as the turbulence decays.

It is found that the size of unstable regions, as measured by the Thorpe scale defined by (3.5), decays to some minimum value for the most stratified cases. This minimum value could be related to a viscous cutoff similar to the cutoff for instability in critical layers. It would be interesting to see at what value of τ_S this lengthscale finally goes to zero, indicating no overturns were measured.

The vertical profiles have been analysed in terms of available potential energy and diapycnal flux. In this framework, fluctuations of the temperature field are compared to the background stable temperature profile. It was found that most of the temperature variability compared to the mean is comprised of stable fluctuations. Therefore, available potential energy, associated only with the unstable fluctuations and turbulent potential energy, defined relative to the mean field, are not strongly correlated, and represent different physical quantities. Further, it was also found that

the stable fluctuations have a Gaussian probability distribution, whereas the unstable fluctuations have a probability distribution with exponential tails.

The diapycnal flux has been compared to the buoyancy flux as the representative rate of mixing in the mean. Though the present results are incomplete, it is clear that diapycnal flux greater than the mean molecular flux can persist while buoyancy flux has collapsed, since enhanced diapycnal flux only requires the existence of scalar fluctuations. It is interesting to note then that fossil turbulence, in which the flow is comprised of only temperature (or density) fluctuations but no turbulent kinetic energy, can also have a diapycnal flux that is greater than the mean molecular flux, even though there is no turbulent mixing.

The present results show that vertical profiles and the framework of background potential energy (Winters *et al.* 1995) can provide additional information about the mixing and structure of the turbulence. Additional investigations are required to validate the balance of energy in equation (3.13) and to understand how diapycnal flux is related to the mean temperature profile evolution.

This work was funded by the Office of Naval Research, Small Scale Physical Oceanography, contract number N000149094-1-0233 and by National Science Foundation Physical Oceanography Grant number OCE 98-71857. We are also indebted to the reviewers for carefully reading our manuscript and making valuable suggestions for its improvement.

Appendix. Correction for diapycnal flux

The diapycnal flux as measured from vertical temperature profiles cannot account for contributions to flux from the spanwise and streamwise directions, since only vertical gradients are measured. In the present investigation, we obtain measurements of

$$\overline{\left(\frac{(\partial T/\partial z)^2}{\mathrm{d}T/\mathrm{d}z_*}\right)} \tag{A 1}$$

instead of

$$\overline{\left(\frac{|\nabla T|^2}{\mathrm{d}T/\mathrm{d}z_*}\right)}. \tag{A 2}$$

where the overbar indicates the expected value and $T = \theta - \bar{T}$, the total temperature. To relate (A 1) to (A 2), we make the approximation

$$\overline{\left(\frac{|\nabla T|^2}{\mathrm{d}T/\mathrm{d}z_*}\right)}\,\overline{\frac{\mathrm{d}T}{\mathrm{d}z_*}} \approx \overline{|\nabla T|^2} \tag{A 3}$$

$$\approx \overline{\left(\frac{\partial\theta}{\partial x}\right)^2} + \overline{\left(\frac{\partial\theta}{\partial y}\right)^2} + \overline{\left(\frac{\partial\theta}{\partial z}\right)^2} + \left(\frac{\mathrm{d}\bar{T}}{\mathrm{d}z}\right)^2. \tag{A 4}$$

The measured ratio $r = \overline{(\partial\theta/\partial z)^2}/\overline{(\partial\theta/\partial x)^2}$ relates the streamwise and vertical mean square gradients, and the spanwise mean square gradient $\overline{(\partial\theta/\partial y)^2}$ is approximated as the average of the vertical and streamwise mean square gradients. Thus,

$$\overline{|\nabla T|^2} \approx \left(\frac{1}{r} + \frac{(1/r)+1}{2} + 1\right)\overline{\left(\frac{\partial\theta}{\partial z}\right)^2} + \left(\frac{\mathrm{d}\bar{T}}{\mathrm{d}z}\right)^2 \tag{A 5}$$

$$\approx \frac{3}{2}\frac{(1+r)}{r}\overline{\left(\frac{\partial\theta}{\partial z}\right)^2} + \left(\frac{\mathrm{d}\bar{T}}{\mathrm{d}z}\right)^2. \tag{A 6}$$

An approximation similar to (A 3) relates the mean square vertical temperature gradient with (A 1):

$$\overline{\left(\frac{(\partial T/\partial z)^2}{\mathrm{d}T/\mathrm{d}z_*}\right)}\ \overline{\frac{\mathrm{d}T}{\mathrm{d}z_*}} \approx \overline{\left(\frac{\partial T}{\partial z}\right)^2} \tag{A 7}$$

$$\approx \overline{\left(\frac{\partial\theta}{\partial z}\right)^2} + \left(\frac{\mathrm{d}\bar{T}}{\mathrm{d}z}\right)^2. \tag{A 8}$$

Taking (A 4, A 6, and A 8), and solving for (A 2) in terms of (A 1) gives

$$\overline{\left(\frac{|\nabla T|^2}{\mathrm{d}T/\mathrm{d}z_*}\right)} \approx \left[\left[\overline{\left(\frac{(\partial T/\partial z)^2}{\mathrm{d}T/\mathrm{d}z_*}\right)}\ \overline{\frac{\mathrm{d}T}{\mathrm{d}z_*}} - \left(\frac{\mathrm{d}\bar{T}}{\mathrm{d}z}\right)^2\right]\frac{3}{2}\frac{(1+r)}{r} + \left(\frac{\mathrm{d}\bar{T}}{\mathrm{d}z}\right)^2\right]\frac{1}{\overline{\mathrm{d}T/\mathrm{d}z_*}}. \tag{A 9}$$

REFERENCES

Baines, P. 1995 *Topographic Effects in Stratified Flows*. Cambridge University Press.

Budwig, R., Tavoularis, S. & Corrsin, S. 1985 Temperature fluctuations and heat flux in grid-generated isotropic turbulence with streamwise and transverse mean temperature gradients. *J. Fluid Mech.* **153**, 441–460.

Chomaz, J. M., Bonneton, P. & Hopfinger, E. J. 1993 The structure of the near wake of a sphere moving horizontally in a stratified fluid. *J. Fluid Mech.* **254**, 1–21.

Christie, S. L. & Domaradzki, J. A. 1994 Scale dependence of the statistical character of turbulent fluctuations in thermal convection. *Phys. Fluids* **6**, 1848–1855.

Davis, R. E. 1994 Diapycnal mixing in the ocean: the Osborn–Cox model. *J. Phys. Oceanogr.* **24**, 2560–2576.

Dillon, T. M. 1982 Vertical overturns: A comparison of Thorpe and Ozmidov length scales. *J. Geophys. Res.* **87**, 9601–9613.

Dillon, T. M. 1984 The energetics of overturning structures: Implications for the theory of fossil turbulence. *J. Phys. Oceanogr.* **14**, 541–549.

Fincham, A. M., Maxworthy, T. & Spedding, G. R. 1996 Energy dissipation and vortex structure in freely decaying, stratified grid turbulence. *Dyn. Atmos. Oceans* **23**, 155–169.

Gargett, A. E. 1989 Ocean turbulence. *Ann. Rev. Fluid Mech.* **21**, 419–451.

Gerz, T., Howell, J. & Mahrt, L. 1994 Vortex structures and microfronts. *Phys. Fluids* **317**, 179–193.

Gerz, T. & Schumann, U. 1996 A possible explanation of countergradient fluxes in homogeneous turbulence. *Theor. Comput. Fluid Dyn.* **8**, 169–181.

Gerz, T., Schumann, U. & Elghobashi, S. E. 1989 Direct numerical simulation of stratified homogeneous turbulent shear flows. *J. Fluid Mech.* **200**, 563–594.

Godeferd, F. S. & Cambon, C. 1994 Detailed investigation of energy transfers in homogeneous stratified turbulence. *Phys. Fluids* **6**, 2084–2100.

Gregg, M. C. 1987 Diapycnal mixing in the thermocline: A review. *J. Geophys. Res.* **92**, 5249–5286.

Haugdahl, J. & Lienhard, J. H. 1988 A low-cost, high-performance DC cold-wire bridge. *J. Phys.* E: *Sci. Instrum.* **21**, 167–170.

Holliday, D. & McIntyre, M. E. 1981 On potential energy density in an incompressible stratified fluid. *J. Fluid Mech.* **107**, 221–225.

Holt, S. E., Koseff, J. R. & Ferziger, J. H. 1992 A numerical study of the evolution and structure of homogeneous stably stratified sheared turbulence. *J. Fluid Mech.* **237**, 499–539.

Hunt, J. C. R. & Carruthers, D. J. 1990 Rapid distortion theory and the 'problems' of turbulence. *J. Fluid Mech.* **212**, 497–532.

Itsweire, E. C. 1984 Measurements of vertical overturns in a stably stratified turbulent flow. *Phys. Fluids* **27**, 764–766.

Itsweire, E. C., Koseff, J. R., Briggs, D. A. & Ferziger, J. H. 1993 Turbulence in stratified shear flows: Implications for interpreting shear-induced mixing in the ocean. *J. Phys. Oceanogr.* **23**, 1508–1522.

Jacobitz, F. G., Sarkar, S. & Van Atta, C. W. 1997 Direct numerical simulations of the turbulence evolution in a uniformly sheared and stably stratified flow. *J. Fluid Mech.* **342**, 231–261.

Keller, K. H. 1999 An experimental investigation of the evolution of turbulent potential and kinetic energies and vertical temperature structure in homogeneous stably stratified sheared turbulence. PhD thesis, University of California, San Diego.

Keller, K. H. & Van Atta, C. W. 2000 Rapid vertical sampling in stably stratified turbulent shear flows. *Dyn. Atmos. Oceans* **31**, 23–45.

Komori, S., Ueda, H., Ogino, F. & Mizushina, T. 1983 Turbulence structure in stably stratified open-channel flow. *J. Fluid Mech.* **130**, 13–26.

LaRue, J. C. Deaton, T. & Gibson, C. H. 1975 Measurement of high-frequency turbulent temperature. *Rev. Sci. Instrum.* **46**, 757–764.

Lienhard, J. H. 1988 The decay of turbulence in a thermally stratified flow. PhD thesis, University of California, San Diego.

Métais, O. & Herring, J. 1989 Numerical simulations of freely evolving turbulence in stably stratified fluids. *J. Fluids Mech.* **202**, 117–148.

Osborn, T. R. & Cox, C. S. 1972 Oceanic fine structure. *Geophys. Fluid Dyn.* **3**, 321–345.

Park, Y.-G., Whitehead, J. A. & Gnanadaskian, A. 1994 Turbulent mixing in stratified fluids: layer formation and energetics. *J. Fluid Mech.* **279**, 279–311.

Piccirillo, P. & Van Atta, C. W. 1996 A multiple-source wind tunnel design for producing turbulent shear flows in a stably stratified fluid. *Exps Fluids* **21**, 66–69.

Piccirillo, P. & Van Atta, C. W. 1997 The evolution of a uniformly sheared thermally stratified turbulent flow. *J. Fluid Mech.* **334**, 61–86.

Rohr, J. J., Itsweire, E. C., Helland, K. N. & Van Atta, C. W. 1988 Growth and decay of turbulence in a stably stratified shear flow. *J. Fluid Mech.* **195**, 77–111.

Salmon, R. 1998 *Lectures on Geophysical Fluid Dynamics*. Oxford University Press.

Staquet, C. 2000 Mixing in a stably-stratified shear layer: two- and three-dimensional numerical experiments. *Fluid Dyn. Res.* submitted.

Staquet, C. & Godeferd, F. S. 1998 Statistical modelling and direct numerical simulations of decaying stably stratified turbulence. Part 1. Flow energetics. *J. Fluid Mech.* **360**, 395–340.

Tavoularis, S. & Corrsin, S. 1981*a* Experiments in nearly homogeneous turbulent shear flow with a uniform mean temperature gradient. Part 1. *J. Fluid Mech.* **104**, 311–347.

Tavoularis, S. & Corrsin, S. 1981*b* Experiments in nearly homogeneous turbulent shear flow with a uniform mean temperature gradient. Part 2. The fine structure. *J. Fluid Mech.* **104**, 349–367.

Taylor, J. R. 1992 The energetics of breaking events in a resonantly forced internal wave field. *J. Fluid Mech.* **239**, 309-340.

Thoroddsen, S. T 1991 Experiments on the statistical nature of stably stratified turbulence. PhD thesis, University of California, San Diego.

Thoroddsen, S. T. & Van Atta, C. W. 1996 Experiments on density-gradient anisotropies and scalar dissipation of turbulence in a stably stratified fluid. *J. Fluid Mech.* **322**, 383–409.

Thorpe, S. A. 1973 Experiments on instability and turbulence in a stratified shear flow. *J. Fluid Mech.* **61**, 731–751.

Warhaft, Z. 2000 Passive scalars in turbulent flows. *Ann. Rev. Fluid Mech.* **32**, 203–240.

Winters, K. B. & D'Asaro, E. A. 1994 Three-dimensional wave instability near a critical level. *J. Fluid Mech.* **272**, 255–284.

Winters, K. B. & D'Asaro, E. A. 1996 Diascalar flux and the rate of fluid mixing. *J. Fluid Mech.* **317**, 179–193.

Winters, K. B., Lombard, P. N., Riley, J. J. & D'Asaro, E. A. 1995 Available potential energy and mixing in density-stratified fluids. *J. Fluid Mech.* **289**, 115–128.